AGU PUBLICATIONS

Geophysical Research Letters

RESEARCH LETTER
10.1002/2015GL066997

Key Points:
- Body and surface wave reconstruction from the VolcArray experiment
- Extraction of body waves propagating through the active magmatic system
- Seismic noise correlation with double beamforming processing

Supporting Information:
- Figures S1–S3

Correspondence to:
N. Nakata,
nnakata@stanford.edu

Citation:
Nakata, N., P. Boué, F. Brenguier, P. Roux, V. Ferrazzini, and M. Campillo (2016), Body and surface wave reconstruction from seismic noise correlations between arrays at Piton de la Fournaise volcano, *Geophys. Res. Lett.*, *43*, 1047–1054, doi:10.1002/2015GL066997.

Received 12 NOV 2015
Accepted 12 JAN 2016
Accepted article online 15 JAN 2016
Published online 1 FEB 2016

Body and surface wave reconstruction from seismic noise correlations between arrays at Piton de la Fournaise volcano

Nori Nakata[1], Pierre Boué[1,2], Florent Brenguier[2], Philippe Roux[2], Valérie Ferrazzini[3], and Michel Campillo[2]

[1]Stanford University, [2]ISTerre, Université Grenoble Alpes, CNRS, Grenoble, France, [3]Observatoire Volcanologique du Piton de la Fournaise/Institut de Physique du Globe de Paris, Sorbonne Paris Cité, CNRS, Paris, France

Abstract Body wave reconstruction from ambient seismic noise correlations is an important step toward improving volcano imaging and monitoring. Here we extract body and surface waves that propagate in Piton de la Fournaise volcano on La Réunion island using ambient noise cross correlation and array-processing techniques. Ambient noise was continuously recorded at three dense arrays, each comprising 49 geophones. To identify and enhance the Green's function from the ambient noise correlation, we apply a double beamforming (DBF) technique between the array pairs. The DBF allows us to separate surface and body waves, direct and reflected waves, and multipathing waves. Based on their azimuths and slownesses, we successfully extract body waves between all the combinations of arrays, including the wave that propagates through the active magmatic system of the volcano. Additionally, we identify the effects of uneven noise source distribution and interpret the surface wave reflections.

1. Introduction

Correlation-based ambient noise techniques are powerful tools for the extraction of wavefields that propagate through the Earth and to obtain static and dynamic elastic parameters of the Earth interiors. Ambient noise surface wave tomography has greatly improved knowledge of subsurface structures [*Shapiro et al.*, 2005; *Roux et al.*, 2011b; *Lee et al.*, 2014]. As the spatial resolution and signal-to-noise ratio (SNR) of correlation functions improve with the number of stations, large numbers of receivers (i.e., hundreds to thousands) have recently been used at both local and global scales [*Mordret et al.*, 2013; *Nishida*, 2013]. When we image and monitor active faults and magmatic reservoirs, body waves provide more accurate information than surface waves because of their spatial resolution and penetration depths. The increase in the number of receivers has an important role for body wave extraction; *Draganov et al.* [2009] obtained reflection images with migration, *Poli et al.* [2012] extracted body waves reflected at the mantle transition zones, and *Nakata et al.* [2015] estimated 3-D *P* wave velocities with body wave tomography.

We use ambient noise data recorded by *VolcArray* at Piton de la Fournaise volcano, La Réunion island [*Brenguier et al.*, 2016], to obtain structural information of the volcanic area (Figure 1). This volcano has been instrumented with many sensors. For example, *Brenguier et al.* [2012] described the deployment of broadband seismometers and GPS networks, *Rivet et al.* [2014] found the long-term changes in seismic velocity and GPS, and *Mordret et al.* [2015] estimated seismic velocities by ambient noise surface wave tomography. In the VolcArray experiment, 299 vertical-component geophones (10 Hz natural frequency) were deployed at 152 locations to continuously observe ground motion for 30 days (July 2014). Each station location was composed of two collocated geophones that were changed around at the middle of the 30 day recording [*Brenguier et al.*, 2016]. Three arrays (Arrays A, B, and C) were located about the same distance (a few kilometers) from the main crater (Dolomieu crater), and each array has 7-by-7 station locations with spacings of about 80 m (Figure 1). The details of this experiment were published by *Brenguier et al.* [2016].

Due to the complexity of volcanoes, identification of the wavefields after cross correlation is not trivial. To understand the correlated wavefields, we use double beamforming (DBF) techniques to fix azimuths and slownesses on both (virtual) source and receiver sides. DBF is an array-processing technique to identify multiple wavefields and/or isolate particular waves from others [*Weber and Wicks*, 1996; *Rost and Thomas*, 2002],

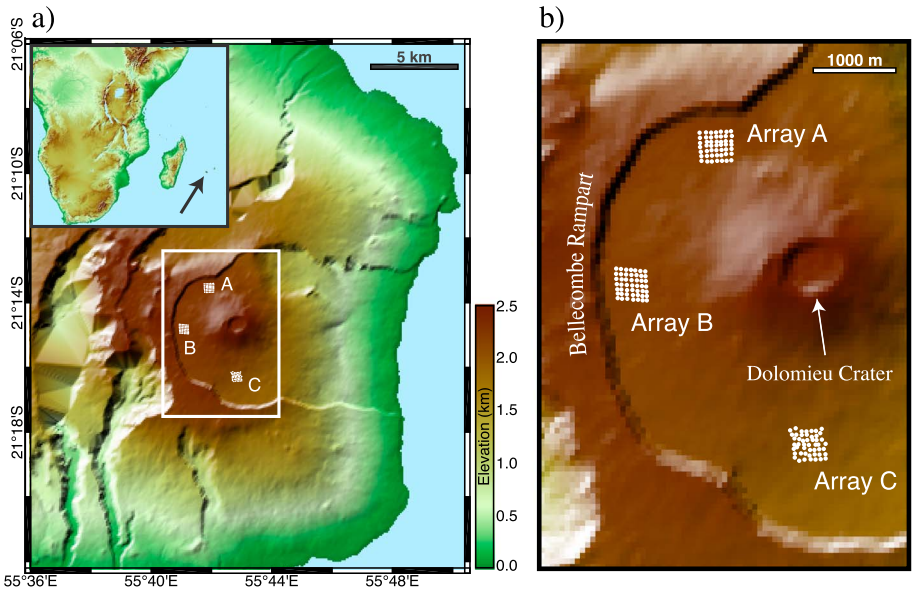

Figure 1. Location of the volcano and receivers. (a) The 152 receivers are deployed as the *VolcArray* experiment, and Arrays A, B, and C have 7-by-7 stations. The inset shows the location of La Réunion island. (b) Magnification of the white rectangle area in Figure 1a. See *Brenguier et al.* [2016] for details about these data.

and its recent use has provided successful results for multipath shallow water tomography [*Roux et al.*, 2008, 2011a]. DBF can identify direct and reflected surface/body waves [*De Cacqueray et al.*, 2011; *Boué et al.*, 2013]. Applying DBF processing to USArray, *Boué et al.* [2014] compensated for the unfavorable noise direction, to improve the accuracy of inverted velocities in ambient noise surface wave tomography. In this study, we apply DBF to correlation functions rather than directly to the observed ambient noise.

The goal of this study is to extract body and surface waves from ambient noise recorded at the volcano while overcoming the complicated wavefields generated by the complex subsurface media and uneven distribution of ambient noise sources. Here we first present the ambient noise correlation averaged over the entire set of observations. Then we decompose the wavefields into the beam domain using DBF to identify direct/scattered body/surface waves. Finally, we show the potential of DBF to improve the SNR of target wavefields.

2. Ambient Noise Correlation

We first downsample the observed signals from 250 Hz to 50 Hz (Nyquist frequency of 25 Hz) to reduce the computational cost. Then we compute the power-normalized cross correlations [i.e., crosscoherence *Nakata et al.*, 2011] between all of the receiver pairs. Taking each receiver in Array A as reference, Figure 2 shows the correlation functions with all other receivers. The traces are summed in equidistant bins while ignoring the azimuth differences between the receiver pairs. The bin size is 20 m with an average of 50 correlations per bin. The traces at distances 0–0.8 km illustrate the correlation functions between the receivers inside Array A. Those at distances 1.8–3.5 km are between the receivers in Arrays A and B. The correlation waveforms between the receivers in Arrays A and C are displayed at distances 4.5–6 km. This stack enhances the coherent part of the correlation functions that can be approximately represented by a simple (e.g., one-dimensional) structural model. The similar correlation functions with reference receivers in Array C are shown in Figure S1 in the supporting information.

After correlation, wavefields contain many signals that are coherent in distance. For example, at 1–3 Hz (Figure 2a), the surface waves propagate with group velocities of 0.5–1 km/s. Faster waves, which are good candidates for body waves, are reconstructed at higher frequencies. Note that the noise processing is performed in a frequency band that is lower than the nominal frequency of the sensors. Because of the stacking procedure involved in both the correlation and the array signal processing, we can enhance the SNR at lower frequencies [e.g., *Nakata et al.*, 2015]. With the complexity of the volcano structure and the uneven distribution of the ambient noise sources, the correlation wavefields are also complicated. Hence, multiple wavelets

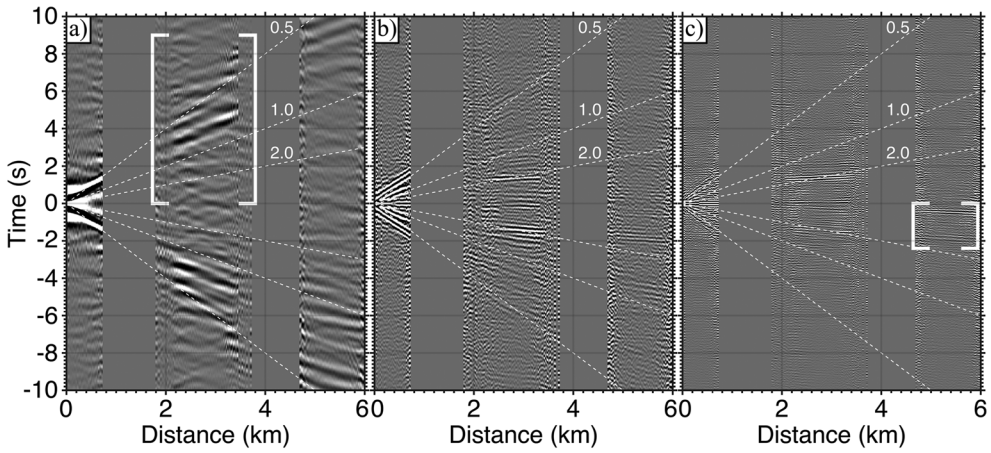

Figure 2. Binned correlation functions between receivers of Array A and all of the receivers at (a) 1–3 Hz, (b) 3–6 Hz, and (c) 6–12 Hz. The distance represents the offset between each receiver pair. Correlations in the positive time indicate outgoing waves from Array A. Because of the survey design, there are no traces at distances 0.8–1.8 km and 3.5–4.5 km. The white dashed lines illustrate the travel times of direct waves with velocities of 0.5, 1, and 2 km/s. We discuss the wavefields highlighted by the white brackets using DBF in Figures 3 and 4.

arrive almost at the same time. The strong-amplitude waves at 0.5 s (Figure 2c, white bracket) might also be puzzling, as these wavelets travel too fast (>10 km/s) if they propagate 5.4 km (the distance from Arrays C to A). Therefore, we use DBF to extract body waves that propagate between all of the array pairs and identify the multiple wavefields that are highlighted by the white brackets in Figure 2. The goal here is not to identify all possible wave paths between each combination of arrays but rather to focus on the dominant waves that can be used for imaging and/or monitoring.

3. Double Beamforming of Correlation Wavefields

3.1. Formulation of Double Beamforming

Consider the computed correlation functions (Figure 2) as functions of the source and receiver locations and time: $\mathfrak{C}(x_s, y_s, x_r, y_r, t)$, where x and y are two independent components in space (e.g., northward and eastward) and s and r refer to the sources and receivers. This expression indicates that (x_s, y_s) represents a source array and (x_r, y_r) a receiver array. For the correlation functions shown in Figure 2, we treat Array A as the (virtual) source array [*Bakulin and Calvert*, 2006]. For beamforming, we use slant-stacking in the time domain, which is relatively simple and easy to implement [*Roux et al.*, 2008; *De Cacqueray et al.*, 2011]. Hence, DBF is based on a plane wave projection, and we can keep wavefields in the time domain. DBF can be considered as a double 2-D *tau-p* transform.

To transform $\mathfrak{C}$ to the double-beam domain, we scan the slowness and azimuth domains at the source and receiver arrays by computing

$$\mathfrak{B}\left(u_s, \theta_s, u_r, \theta_r, t\right) = \frac{1}{N_s N_r} \sum_{x_s} \sum_{y_s} \sum_{x_r} \sum_{y_r} \mathfrak{C}\left(x_s, y_s, x_r, y_r, t - \tau_s\left(x_s, y_s, u_s, \theta_s\right) + \tau_r\left(x_r, y_r, u_r, \theta_r\right)\right), \quad (1)$$

where τ is the time lag that corresponds to source/receiver location, slowness (u), and azimuth (θ), and N is the number of sources and receivers ($N_s = N_r = 49$). The azimuths at the source and receiver arrays are defined by the outgoing and incoming waves relative to the north direction, respectively (see Figure 3, inset). Instead of using u and θ, we can modify equation (1) with slownesses in the x and y directions ($[u_x, u_y] = [u \sin\theta, u \cos\theta]$). The time lag τ is a relative time delay from a reference point. We set the reference at the center of each array (x^c, y^c), and thus, the time lag τ_s is defined as

$$\tau_s = u_s\left(x_s - x_s^c\right)\sin\theta_s + u_s\left(y_s - y_s^c\right)\cos\theta_s, \quad (2)$$

and similar formula for τ_r. Due to the summation (equation (1)), we improve the SNR by at most $\sqrt{N_s N_r}$ compared to the point-by-point correlation ($\mathfrak{C}$) when the signal is plane waves and the noise is white. Therefore, a large number of receivers are helpful to enhance target waves.

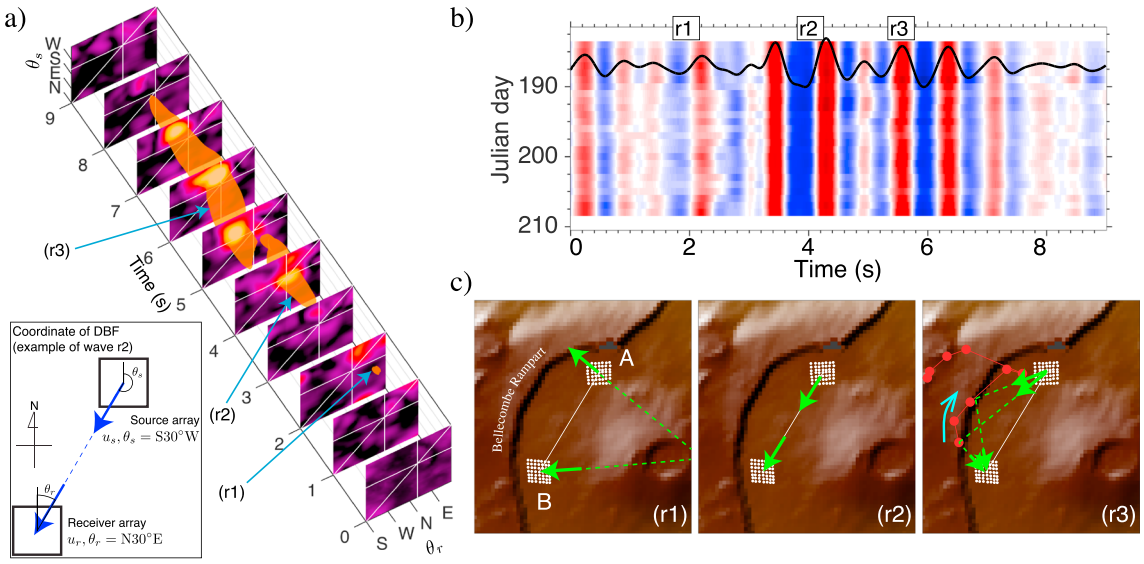

Figure 3. (a) Time slices and isointensity surfaces (orange) of the envelope of DBF correlations highlighted by the white bracket in Figure 2a (1–3 Hz). The bright color indicates higher intensity. The convention for DBF is defined in the lower-left inset. The azimuth of the source array depends on the outgoing waves and that of the receiver array on the incoming waves. The vertical and horizontal white lines are the azimuths of the direct path on the receiver and source arrays, respectively. To illustrate the DBF envelope, we fix two parameters out of five in the beam domain: $\mathfrak{B}(u_s = 0.96$ s/km (≈1.04 km/s), θ_s, $u_r = 0.96$ s/km, θ_r, $t)$. The blue arrows highlight the higher intensity waves shown with isosurfaces (waves r1–r3). (b) DBF waveforms for the direct path from Arrays A to B ($\mathfrak{B}(u_s = 0.96$ s/km, $\theta_s = $ S30°W, $u_r = 0.96$ s/km, $\theta_r = $ N30°E, $t)$). The background images show the daily waveforms and the black lines the averaged waveforms over all of the days. (c) Outgoing/incoming angles of surface waves propagating from Array A to Array B obtained by DBF analysis. Each panel corresponds to waves r1–r3, respectively. The green solid arrows indicate the measured azimuths of the surface waves in Figure 3a. The red dots indicate the reflection points for each 0.25 s between 5 and 7 s estimated by DBF with a straight-ray assumption, and the blue arrow in Figure 3c indicates the migration of the reflection points with time.

The slowness measured with a 2-D array on the surface is the inverse of the phase velocity for surface waves and of the local apparent velocity for body waves. Dense arrays have an important role for DBF to avoid aliasing artifacts [*Roux et al.*, 2008]. In VolcArray, the Nyquist wavenumber k_n is $k_n = 2\pi u_n f_n = 2\pi/2\Delta x$, where f is the frequency and Δx is the minimum station spacing, which is about 85 m in the grid directions (as directions approximately east and north). Therefore, spatial aliasing occurs when $uf > 5.88$ km^{-1} in these directions. As aliasing is frequency dependent, it is less significant when we average over a wide frequency range (e.g., 1–3 Hz). The slowness resolution Δu in the grid directions is $\Delta uf = 1.0$ km^{-1} as the array size is 0.5×0.5 km^2. The frequency-dependent array response at each array was shown by *Brenguier et al.* [2016].

3.2. Surface Waves

First, we use DBF to identify the correlation wavefields at 1–3 Hz (wavefields highlighted by the white bracket in Figures 2a and 3). To illustrate the 5-D object $\mathfrak{B}$, we fix $u_s = u_r = 0.96$ s/km (≈1.04 km/s) to maximize the power of the envelope, and we plot the envelope as a function of time and azimuth (Figure 3a). Due to the velocity of high-intensity areas (Figure 3a, orange surface) and the frequency range (1–3 Hz), we consider these waves as Rayleigh waves. The phase velocities are about 1.0 km/s and 0.6 km/s at 1.5 Hz and 2.7 Hz, respectively (not shown as figures). Based on the model of *Mordret et al.* [2015], the sensitivity of these surface waves is a few hundred meters deep.

We find three high-intensity waves (Figure 3a, r1, r2, r3). Wave r2 propagates along the direct path with a group velocity of about 0.7 km/s (Figure 3c). Figure 3b shows the seismograms at the azimuth of the direct path. Based on the daily waveforms, three waves are coherently reconstructed.

At 4.5 s, waves start propagating at different azimuths. Note that the intensity isosurfaces of waves r2 and r3 are not continuous (Figure 3a). Wave r3 is a surface wave reflected at the Bellecombe rampart (Figure 3c). The change in azimuth of wave r3 with time indicates that the reflection points are shifting northward (Figure 3c, red dots, blue arrow), which is consistent with lengthening of the travel paths along the blue arrow. The reflection points are estimated from the intersection of the straight lines with the azimuths estimated by DBF at the source and receiver arrays. As the ambient noise intensity arrives at Array A stronger from the east than the north [*Brenguier et al.*, 2016], the intensity of the reflected waves is also strong. After 6 s, the reflection points

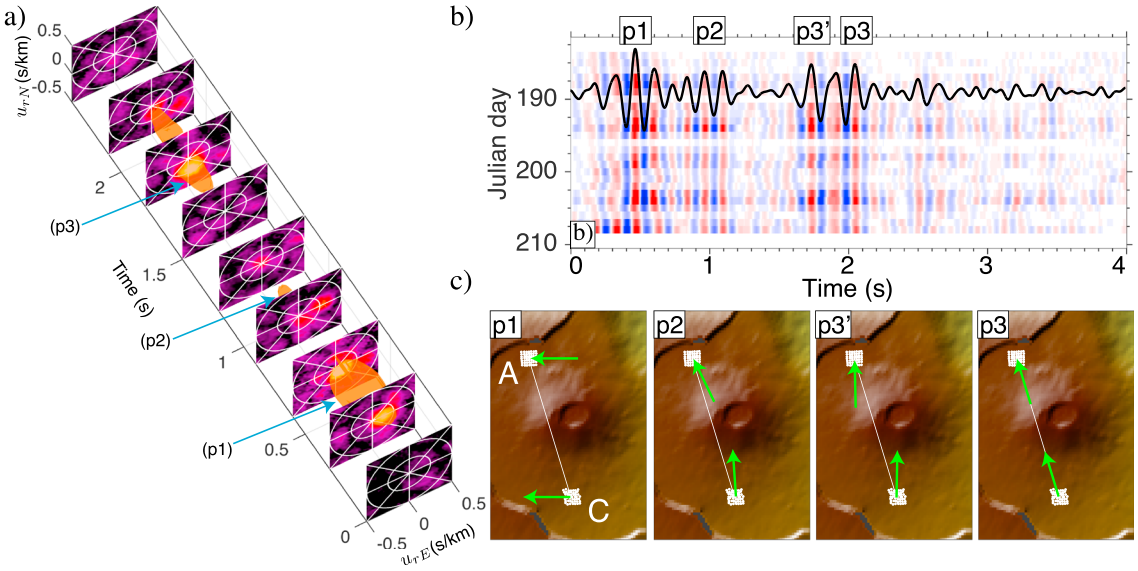

Figure 4. As for Figure 3, but for the waves in the white bracket in Figure 2c (6–12 Hz). We treat Array C as the source array because the time window used in Figure 2c is in negative time. The white circles in Figure 4a indicate the horizontal slownesses of 0.25 and 0.5 s/km (= 4.0 and 2.0 km/s, respectively). To illustrate the DBF envelope (Figure 4a), we fix the source-array parameters into the direct *P* wave region ($\mathfrak{B}(u_s = 0.20$ s/km (≈5.0 km/s), θ_s = N20°W, $u_r, \theta_r, t)$) and convert u_r and θ_r to northward and eastward slownesses u_{rN} and u_{rE}, respectively. The DBF waveforms at the direct *P* wave angles and slownesses are shown in Figure 4b., and waves p1–p3 are illustrated in Figure 4c.

move toward the west (the last four red points). We speculate that the reflections are caused by the geological structure of the volcano at the point where the topography changes.

These inferred reflection paths and their arrival times suggest that the velocities inside and outside the Bellecombe rampart are very different. The lengths of the ray paths of waves arriving at 5.0 s (Figure 3c, first red dot) and 6.25 s (first red dot outside the rampart) are approximately 3.6 km and 5.5 km, respectively, and the corresponding group velocities are 0.72 km/s and 0.88 km/s, respectively. The velocity of 0.72 km/s is nearly equal to that estimated from the direct waves (0.70 km/s), because the reflected waves travel only inside the rampart. As the velocity of 0.88 km/s is much faster than the velocity inside the rampart, the velocity outside the rampart is significantly faster. This difference corresponds well with the velocities estimated by *Mordret et al.* [2015]. In contrast from *Mordret et al.* [2015], we do not use stations outside the rampart, but we can still obtain velocity information there by using array processing. Also, reflections have the potential to image velocity boundaries more sharply than transmitted wave tomography.

The wave r1, which arrives at an early time, is caused by directional noise sources (i.e., anisotropy of noise energy) on the east side of the arrays (Figure 3c). The noise sources are related to either the volcanic activities or the ocean (see Figure 1). Due to smearing and the limits of resolution, we cannot completely mute waves r1 and r3 in Figure 3b. However, these waves are weaker after DBF processing than the point-by-point correlation wavefields. Importantly, we can identify these waves as nondirect surface waves. For imaging/monitoring between arrays, these waves can be considered as artifacts (also known as spurious waves) that do not participate in the construction of the Green's function [e.g., *Wapenaar and Fokkema*, 2006]. Without DBF or other array-processing methods, we cannot recognize these artifacts. This indicates that DBF can separate the noise sources based on their directionality in the correlation functions, which is helpful for the extraction of the wavefields propagating between two arrays and for reducing any bias of images potentially caused by spurious waves.

3.3. Body Waves

Next, we analyze waves at higher frequencies (Figure 2c, white bracket, and Figure 4). We compute the 5-D object $\mathfrak{B}$, and for display purposes, we fix the slowness and azimuth at the source array in Figure 4a (u_s= 0.20 s/km (≈5.0 km/s) and θ_s = N20°W). Due to their frequency and slowness, we interpret the coherent waves in Figure 2c as *P* waves. Figure 4b shows the waveforms at the direct *P* wave paths on both the source and receiver array sides.

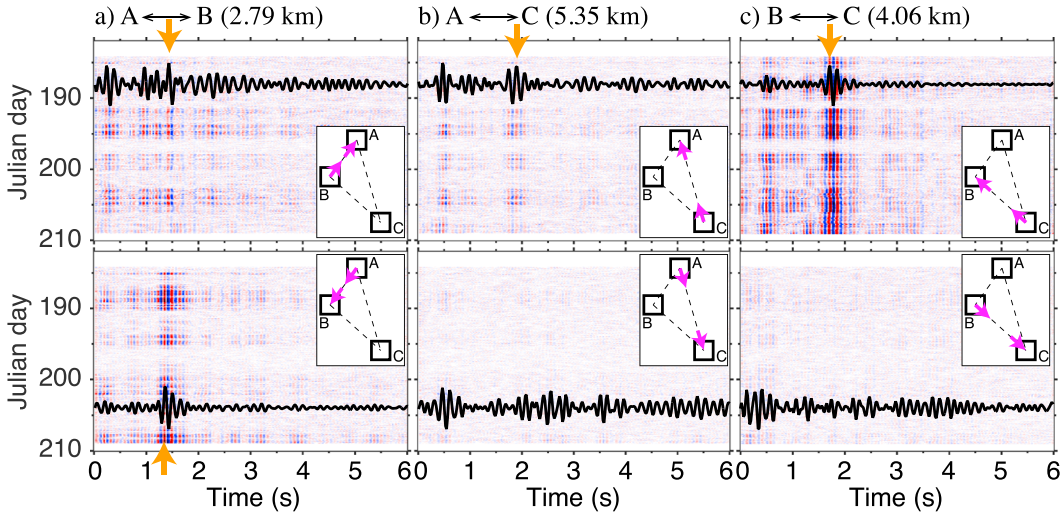

Figure 5. DBF wavefields along the azimuth of direct paths between the source and receiver arrays at 6–12 Hz after averaging over the DBF contributions with wave velocities greater than 1.5 km/s. In each panel, the background image shows hourly DBF wavefields, the black line indicates the stacked waveforms over all hourly functions, and the inset illustrates the azimuths used for DBF. The distances are measured between the central points at each array pair. The orange arrows highlight the direct body waves.

Similar to wave r1 in Figure 3, wave p1 is related to strong noise sources from the east (Figure 4c). Because the noise on the east side is strong and due to the limitation of resolution, wave p1 remains as an artifact after applying DBF. Based on waves r1 and p1, seismic noise for both surface and body waves dominantly propagates from east, which is consistent with *Brenguier et al.* [2016]. Note that the resolution of the azimuth at high apparent velocities is not as high as at low apparent velocities.

Wave p3 is interpreted as the body wave directly traveling between Arrays C and A with an apparent velocity of 5.0 km/s (Figures 4a and 4c). Based on ray theory with an assumption of laterally homogeneous media, the apparent velocity of 5.0 km/s corresponds to the velocity of the rock mass at the turning point of the ray. Hence, this wave travels below the active central crater and reaches the level of the seismically active region at between 1 and 2 km in depth [*Peltier et al.*, 2009]. This high velocity corresponds to the velocity of slowly solidified basaltic intrusive magma bodies. These results are in agreement with *Prôno et al.* [2009], and these waves are useful for more accurate estimates of the sharp velocity contrast between shallow low-velocity cooled lava piles and a deeper intrusive high-velocity magma body. More data would be necessary to precisely assess the depth of this high-velocity intrusive body. This high-velocity intrusive magma body where seismicity occurs probably acts as a cap rock for the shallow magma reservoir located at about sea level [*Peltier et al.*, 2009].

Wave p2 also propagates along the nearly direct path with almost the same apparent velocity as wave p3, although its travel time is about the half of the time for wave p3. We speculate that wave p2 is constructed from the correlation of head wave noise traveling at the depth of the layer of the velocity of 5.0 km/s, where wave p3 also reaches (similar to *Mikesell and van Wijk* [2011]). The arrival time of wave p2 (~ 1 s) can be explained by the travel time of the wave along the layer (5.4 km/5.0 km/s). Although dense arrays are critical for distinguishing fast body waves without spatial aliasing, larger array aperture might be helpful for further understanding wave p2.

Figure 4b shows another coherent wave p3′ at 1.8 s. According to the DBF analysis, the azimuth of the wave p3′ is at about 25° from the direct path on both source and receiver sides. We interpret that wave p3′ is caused by another dominant noise energy coming from almost south [*Brenguier et al.*, 2016]. With scattering of wavefields and DBF, we can extract and enhance the wave p3.

With DBF, we can improve the SNR of the body waves. In Figure 5, we enhance the SNR of direct body waves between each array pair by using only θ_s and θ_r along the direct ray path and averaging over the DBF contributions with wave velocities greater than 1.5 km/s. To show the stability of the extracted waves, we compute the hourly DBF. We observe clear arrivals for different array combinations from the 1 h data. Because of the directionality of ambient noise [*Brenguier et al.*, 2016], body waves have good SNR in one direction (C to A and

C to B) but not in the other (A to C and B to C). The fluctuations in the amplitudes of the body waves over a month (e.g., weak amplitudes on day 190 and 197 in C to B) are related to the variations in noise directionality and its energy.

The arrival times of the waves are 1.3 s between A and B, 2.0 s between A and C, and 1.7 s between B and C (Figure 5, orange arrows). These arrival times are larger than the predicted times (0.9 s, 1.46 s, and 1.36 s at A–B, A–C, and B–C, respectively) based on the velocity model used for earthquake locations by the Piton de la Fournaise volcano observatory (OVPF). The velocity model used for computing the predicted travel times was obtained through earthquake-based tomography [*Prôno et al.*, 2009]. This model is thus poorly resolved over the first 2 km depth; the surface velocity is about 3.5 km/s. However, the direct *P* waves that we reconstruct with DBF travel mostly in these first 2 km. Our observations thus demonstrate that the near surface of the volcano shows *P* wave velocities about 10% lower than what was expected from earthquake-based tomography. This corroborates results of near-surface surface wave tomography at Piton de la Fournaise volcano [*Brenguier et al.*, 2007] and demonstrates the interest of noise-based *P* wave tomography for improving near-surface velocity models, and in this case, a volcanic seismic event location.

As the hourly DBF waveforms show clear body waves (Figure 5), we can increase the temporal resolution of the correlation functions, which is important for monitoring purposes. For comparison, we show hourly correlation functions computed from single receiver pairs (Figure S2) and from binned point-by-point correlations (Figure S3). Single-receiver pairs are not enough to extract clear body waves even after averaging over the entire observation time. The binned correlations reconstruct the body waves propagating from C to B and A to B but not for other combinations. Note that the SNR of the reconstructed hourly body waves is not as high as with DBF. In addition, we enhance the stability of direct body waves with DBF. For example, the body waves on days 200–203 that propagate from C to B are more stable with DBF (Figure 5c, orange arrow) than with the binned stacks (Figure S3c).

Measurements of temporal changes at volcanoes provide important information about the volcanic activity [*Brenguier et al.*, 2008]. DBF of dense arrays reduces the influence of noise source directionality and thus can improve the ability to detect the changes in seismic velocities of the volcano. Note that we do not observe any significant volcanic activity around this time interval.

4. Conclusion

We apply cross correlation and DBF processing to continuous ambient noise records to extract body waves at Piton de la Fournaise volcano. Through the use of slowness and azimuth, DBF is powerful for the identification of the correlation wavefields compared to averaged point-by-point correlations. With DBF, we find body waves with multipaths as well as direct and reflected surface waves. Also, we distinguish the waves related to stationary phases and separate these from spurious waves caused by the noise distribution. Here we demonstrate the use of DBF to characterize correlation wavefields, and we can repeat the similar analysis for every coherent wave in Figure 2. Because of the complex structures of volcanoes, multipath body waves arrive almost simultaneously. DBF can separate these waves and/or increase their SNR. One application of these DBF-extracted body waves is temporal monitoring, because the SNR of the daily/hourly waveforms is stable. Another application might be body wave tomography at the volcano, but this would require better sensor coverage.

Acknowledgments

VolcArray is a joint project between ISTerre, OVPF, IPGP, and Parc National de La Réunion. It was funded by Foundation Simone and Cino Del Duca (Institut de France), La Ville de Paris (projet Emergences), European Research Council through Advanced grant 227507 Whisper, and the Service National d'Observation en Volcanologie with support from the company FairFieldNodal. The data and metadata are available without restrictions from the RESIF and EIDA data centers under the FDSN network code XP (doi:10.15778/RESIF.XP2014). The computer resources for the processes were provided by the Center for Computational Earth and Environmental Science at Stanford University and SuperMicro Computer, Inc. Nori Nakata acknowledges the financial support of the George Thompson Fellowship at Stanford University. We are grateful for John Hole and one anonymous reviewer for their comments. ISTerre is part of Labex OSUG@2020 (ANR10 LABX56).

References

Bakulin, A., and R. Calvert (2006), The virtual source method: Theory and case study, *Geophysics*, *71*(4), SI139–SI150.

Boué, P., P. Roux, M. Campillo, and B. de Cacqueray (2013), Double beamforming processing in a seismic prospecting context, *Geophysics*, *78*(3), V101–V108.

Boué, P., P. Roux, M. Campillo, and X. Briand (2014), Phase velocity tomography of surface waves using ambient noise cross correlation and array processing, *J. Geophys. Res. Solid Earth*, *119*, 519–529, doi:10.1002/2013JB010446.

Brenguier, F., N. M. Shapiro, M. Campillo, A. Nercessian, and V. Ferrazzini (2007), 3-D surface wave tomography of the Piton de la Fournaise volcano using seismic noise correlations, *Geophys. Res. Lett.*, *34*, L02305, doi:10.1029/2006GL028586.

Brenguier, F., N. M. Shapiro, M. Campllo, V. Ferrazzini, Z. Duputel, O. Coutant, and A. Nercessian (2008), Towards forecasting volcanic eruptions using seimsic noise, *Nat. Geosci.*, *1*, 126–130.

Brenguier, F., et al. (2012), First results from the UnderVolc high resolution seismic and GPS network deployed on Piton de la Fournaise Volcano, *Seismol. Res. Lett.*, *83*, 97–102.

Brenguier, F., et al. (2016), Towards 4-D noise-based seismology: First results of a Large-N array experiment on Piton de la Fournaise volcano, *Seismol. Res. Lett.*, *87*(1), 15–25, doi:10.1785/0220150173.

De Cacqueray, B., P. Roux, M. Campillo, S. Catheline, and P. Boué (2011), Elastic-wave identification and extraction through array processing: An experimental investigation at the laboratory scale, *J. Appl. Geophys.*, *74*, 81–88.

Draganov, D., X. Campman, J. Thorbecke, A. Verdel, and K. Wapenaar (2009), Reflection images from ambient seismic noise, *Geophysics*, *74*(5), A6–A67.
Lee, E.-J., P. Chen, T. H. Jordan, P. B. Maechling, M. A. M. Denolle, and G. C. Beroza (2014), Full-3-D tomography for crustal structure in Southern California based on the scattering-integral and the adjoint-wavefield methods, *J. Geophys. Res. Solid Earth*, *119*, 6421–6451, doi:10.1002/2014JB011346.
Mikesell, D., and K. van Wijk (2011), Seismic refraction interferometry with a semblance analysis on the crosscorrelation gather, *Geophysics*, *76*(5), SA77–SA82.
Mordret, A., M. Landès, N. M. Shapiro, C. Singh, P. Roux, and O. I. Barkved (2013), Near-surface study at the Valhall oil field from ambient noise surface wave tomography, *Geophys. J. Int.*, *193*, 1627–1643.
Mordret, A., D. Rivet, M. Landés, and N. M. Shapiro (2015), Three-dimensional shear velocity anisotropic model of Piton de la Fournaise Volcano (La Réunion Island) from ambient seismic noise, *J. Geophys. Res. Solid Earth*, *1*, 406–427, doi:10.1002/2014JB011654.
Nakata, N., R. Snieder, T. Tsuji, K. Larner, and T. Matsuoka (2011), Shear-wave imaging from traffic noise using seismic interferometry by cross-coherence, *Geophysics*, *76*(6), SA97–SA106, doi:10.1190/GEO2010-0188.1.
Nakata, N., J. P. Chang, J. F. Lawrence, and P. Boué (2015), Body wave extraction and tomography at Long Beach, California, with ambient-noise interferometry, *J. Geophys. Res. Solid Earth*, *120*, 1159–1173, doi:10.1002/2015JB01870.
Nishida, K. (2013), Global propagation of body waves revealed by cross-correlation analysis of seismic hum, *Geophys. Res. Lett.*, *40*, 1691–1696, doi:10.1002/grl.50269.
Peltier, A., P. Bachéley, and T. Staudacher (2009), Magma transport and storage at Piton de La Fournaise (La Réunion) between 1972 and 2007: A review of geophysical and geochemical data, *J. Volcanol. Geotherm. Res.*, *184*(1), 93–108.
Poli, P., M. Campillo, H. Pedersen, and L. W. Group (2012), Body-wave imaging of Earth's mantle discontinuities from ambient seismic noise, *Science*, *338*, 1063–1065.
Prôno, E., J. Battaglia, V. Monteiller, J.-L. Got, and V. Ferrazzini (2009), P-wave velocity structure of Piton de la Fournaise volcano deduced from seismic data recorded between 1996 and 1999, *J. Volcanol. Geotherm. Res.*, *184*, 49–62.
Rivet, D., F. Brenguier, D. Clarke, N. M. Shapiro, and A. Peltier (2014), Long-term dynamics of Piton de la Fournaise volcano from 13 years of seismic velocity change measurements and GPS observations, *J. Geophys. Res. Solid Earth*, *119*, 7654–7666, doi:10.1002/2014JB011307.
Rost, S., and C. Thomas (2002), Array seismology: Methods and applications, *Rev. Geophys.*, *40*(3), 1008, doi:10.1029/2000RG000100.
Roux, P., B. D. Cornuelle, W. A. Kuperman, and W. S. Hodgkiss (2008), The structure of raylike arrivals in a shallow-water waveguide, *J. Acoust. Soc. Am.*, *124*, 3430–3439.
Roux, P., I. Iturbe, B. Nicolas, J. Virieux, and J. I. Mars (2011a), Travel-time tomography in shallow water: Experimental demonstration at an ultrasonic scale, *J. Acoust. Soc. Am.*, *130*, 1232–1241.
Roux, P., M. Wathelet, and A. Roueff (2011b), The San Andreas Fault revisited through seismic-noise and surface-wave tomography, *Geophys. Res. Lett.*, *38*, L13319, doi:10.1029/2011GL047811.
Shapiro, N. M., M. Campillo, L. Stehly, and M. H. Ritzwoller (2005), High-resolution surface-wave tomography from ambient seismic noise, *Science*, *307*, 1615–1618.
Wapenaar, K., and J. Fokkema (2006), Green's function representations for seismic interferometry, *Geophysics*, *71*(4), SI33–SI46.
Weber, M., and C. W. Wicks (1996), Reflections from a distant subduction zone, *Geophys. Res. Lett.*, *23*(12), 1453–1456.